

## MATERIALS SCIENCE

## Engineering stable interfaces for three-dimensional lithium metal anodes

Jin Xie<sup>1\*</sup>, Jiangyan Wang<sup>1\*</sup>, Hye Ryoung Lee<sup>1</sup>, Kai Yan<sup>1</sup>, Yuzhang Li<sup>1</sup>, Feifei Shi<sup>1</sup>, William Huang<sup>1</sup>, Allen Pei<sup>1</sup>, Gilbert Chen<sup>1</sup>, Ram Subbaraman<sup>2</sup>, Jake Christensen<sup>2</sup>, Yi Cui<sup>1,3†</sup>

Lithium metal has long been considered one of the most promising anode materials for advanced lithium batteries (for example, Li-S and Li-O<sub>2</sub>), which could offer significantly improved energy density compared to state-of-the-art lithium ion batteries. Despite decades of intense research efforts, its commercialization remains limited by poor cyclability and safety concerns of lithium metal anodes. One root cause is the parasitic reaction between metallic lithium and the organic liquid electrolyte, resulting in continuous formation of an unstable solid electrolyte interphase, which consumes both active lithium and electrolyte. Until now, it has been challenging to completely shut down the parasitic reaction. We find that a thin-layer coating applied through atomic layer deposition on a hollow carbon host guides lithium deposition inside the hollow carbon sphere and simultaneously prevents electrolyte infiltration by sealing pinholes on the shell of the hollow carbon sphere. By encapsulating lithium inside the stable host, parasitic reactions are prevented, resulting in impressive cycling behavior. We report more than 500 cycles at a high coulombic efficiency of 99% in an ether-based electrolyte at a cycling rate of 0.5 mA/cm<sup>2</sup> and a cycling capacity of 1 mAh/cm<sup>2</sup>, which is among the most stable Li anodes reported so far.

## INTRODUCTION

Recent developments in consumer electronics, electric vehicles, and grid-scale energy storage necessitate energy storage with high energy/power densities. Among candidate technologies, Li-S and Li-O<sub>2</sub> batteries have attracted particular attention due to their high theoretical energy densities (1–4). With the highest specific capacity of 3860 mAh/g and the lowest electrochemical potential among anode materials, lithium metal is considered the most promising anode for both Li-S and Li-O<sub>2</sub> (5, 6). However, despite decades of intense research and development efforts, the commercialization of lithium metal batteries remains hindered by poor long-term stability and concerns over their safety.

The key challenges facing lithium metal anodes are (i) high chemical reactivity of lithium with the liquid electrolyte and (ii) infinite relative volume change during lithium plating/stripping (6). With the most negative electrochemical potential, lithium metal is able to reduce common organic electrolytes upon contact, leading to the formation of a solid electrolyte interphase (SEI) at the electrode/electrolyte interface (7, 8). In addition, the extreme volume change during lithium plating/stripping fractures this, typically mechanically fragile SEI, resulting in the exposure of highly reactive fresh lithium to the electrolyte to form new SEI. The continuous fracture and formation of the SEI during battery cycling lead to the consumption of active lithium and electrolyte, resulting in capacity fade and impedance rise (5, 6). This motivates the design of three-dimensional (3D) lithium hosts with stable interfaces to (i) guide lithium plating/stripping, (ii) form a stable SEI, and (iii) prevent lithium from reacting with the electrolyte, all of which are essential

to the development of lithium metal-based batteries with high coulombic efficiency and long cycle life.

Of the various approaches to maximizing lithium metal anode performance, design of lithium hosts to accommodate the large volume change of lithium during cycling along with development of stable interfaces to minimize parasitic reactions are the most promising. The majority of lithium hosts reported so far can be divided into two main categories. The first type of lithium host is prepared by a thermal overlithiation reaction with lithiophilic substrates (9–11). By adjusting the lithium affinity of the high-surface area substrates, molten lithium can infiltrate lithiophilic substrates. While they have been shown to suppress lithium dendrite formation in the bulk, especially under high current densities, lithium infiltration pathways on the surface remain exposed, which leaves the lithium inside the host vulnerable to electrolyte reactions. A second type of lithium hosts consists of hollow electrodes that can accommodate electrochemically plated lithium (12, 13). However, the preparation of hollow hosts via template-assisted methods requires subsequent removal of templates, which inevitably leaves micropores on the shell (14, 15). Therefore, it is essential to prepare a stable interface on the surface of lithium hosts to completely seal pathways for the electrolyte to react with lithium. Toward this goal, many types of artificial interfaces have been studied, including oxides (16–18), fluorides (19, 20), phosphates (21, 22), 2D materials (23, 24), and ceramic solid electrolytes (25). Among them, atomic layer deposition (ALD) has recently emerged as a particularly promising tool because it enables pinhole-free coatings on high-aspect ratio lithium battery electrodes (16, 17, 26, 27).

Here, we designed and developed a novel 3D electrode using ALD-coated hollow carbon spheres (HCS). The microporous carbon shell acts as a mechanically sturdy frame to confine electrochemical lithium plating. Compared to our previous study (12), a new advancement of the thin ALD coating seals the micropores of HCS to keep the electrolyte from contacting lithium and deactivates defective HCS surfaces (Fig. 1). Through this design, the liquid electrolyte only contacts the outer surface of ALD Al<sub>2</sub>O<sub>3</sub>/HCS and cannot

<sup>1</sup>Department of Materials Science and Engineering, Stanford University, Stanford, CA 94305, USA. <sup>2</sup>Bosch Research and Technology Center North America, 4005 Miranda Avenue #200, Palo Alto, CA 94304, USA. <sup>3</sup>Stanford Institute for Materials and Energy Sciences, SLAC National Accelerator Laboratory, 2575 Sand Hill Road, Menlo Park, CA 94025, USA.

\*These authors contributed equally to this work.

†Corresponding author. Email: yicui@stanford.edu

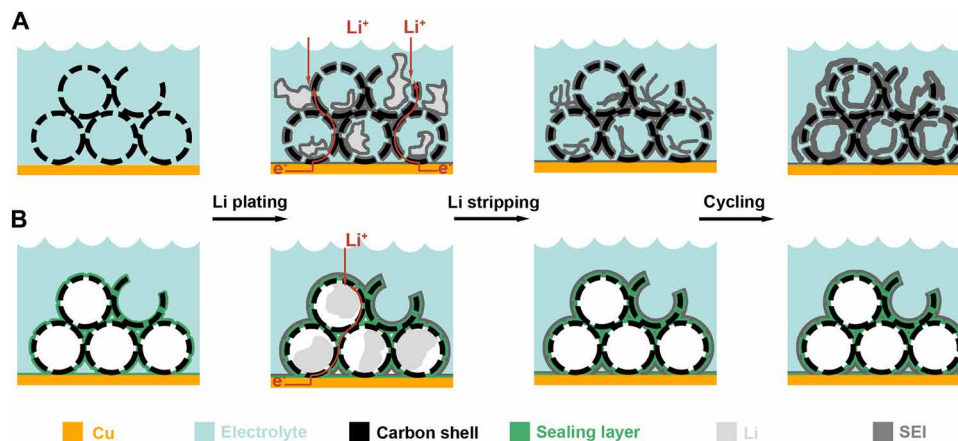


**Fig. 1. Schematic of lithium plating/stripping in lithium hosts.** (A) Without a sealing layer, the electrolyte penetrates inside the pores of the lithium host and lithium deposition is uncontrolled. A thin layer of SEI forms on the surface of both the lithium and the lithium host. During stripping, the SEI on the lithium surface can break and accumulate in the electrode. In later cycles, SEI continues to break and form, resulting in a very thick SEI layer. The side reactions consume both active lithium and electrolyte, leading to battery failure. (B) A uniform sealant layer encapsulates the lithium host, preventing electrolyte penetration and guiding lithium deposition inside the host. A thin and stable SEI is then grown outside the lithium host upon cycling.

penetrate the hollow sphere. Therefore, SEI forms only on the outside of the ALD-coated HCS upon cycling. During lithium deposition, lithium ions penetrate the outer  $\text{Al}_2\text{O}_3/\text{C}$  shell and are plated inside the hollow sphere. An impressive cycling behavior with more than 500 cycles at a high coulombic efficiency of 99% was achieved in the ether-based electrolyte, which is superior to most previous work under similar testing conditions.

## RESULTS

### Synthesis and characterizations of ALD $\text{Al}_2\text{O}_3/\text{HCS}$

As a proof of concept of our sealed host, we use HCS as our lithium host due to its high electrical conductivity, excellent chemical stability in the electrolyte, low cost, and scalable synthesis (Fig. 2A). Briefly, HCS was prepared via a hard-template method. The  $\text{SiO}_2$  nanoparticle templates with an average diameter of 645 nm were prepared using the Stöber method (Fig. 2B; see also Materials and Methods for more details of synthesis procedures). The carbon shell was prepared by first coating the  $\text{SiO}_2$  templates with resorcinol-formaldehyde (RF) resin and subsequently calcining in an Ar environment at  $800^\circ\text{C}$ . The  $\text{SiO}_2$  template was then etched in HF aqueous solution, leaving only the carbon shell. The carbon shell prepared by this method is nanoporous (28–30), as a result of the vapor by-product generated in the calcination process. Despite the continuous surface implied by electron micrographs (Fig. 2, C and E), the carbon shell has sub-2 nm pores (29), which allow HF to enter the HCS and etch the  $\text{SiO}_2$  template [see also scanning electron microscopy (SEM) images after different etching times in the Supplementary Materials]. These nanopores serve as a double-edged sword; on one hand, they allow the  $\text{SiO}_2$  templates to be removed; on the other hand, they also allow penetration of the organic electrolyte during battery operation, which reacts with lithium to reduce the battery cycling performance. These nanopores are intrinsic to almost all template-assisted hollow nanostructures as they are the mechanism by which the template is removed (14, 15). For use as a host for lithium metal, these pinholes must be sealed to prevent parasitic side reactions. Of various candidate methods, ALD is advantageous due to its excellent coverage and fine control

over the film thickness. Because of the slow diffusion of precursor gases through the HCS nanopores, deposition can be regulated primarily outside of the HCS by controlling the precursor residence time inside the deposition chamber during each cycle (31, 32). Both  $\text{Al}_2\text{O}_3$  and  $\text{AlF}_3$  (see Materials and Methods) have been investigated as coating layers on HCS and exhibited core-shell structures confirmed by scanning transmission electron microscopy (STEM)–energy-dispersive x-ray (EDX) (Fig. 2E and the Supplementary Materials). This demonstrates the ability and versatility of ALD to coat various materials to serve as lithium hosts for battery applications.

### Suppression of electrolyte penetration and regulation of lithium plating

The HF etching experiment (see the Supplementary Materials) suggests that liquids can slowly infiltrate the pores of HCS. To further validate and visualize electrolyte infiltration, we performed SEM/FIB (focused ion beam) characterization of HCS electrodes and ALD  $\text{Al}_2\text{O}_3/\text{HCS}$  electrodes dried in different solutions. Two types of solutions were selected: (i) the battery electrolyte ethylene carbonate (EC)/diethyl carbonate (DEC) with 1 M  $\text{LiPF}_6$  and (ii) saturated  $\text{NaCl}/\text{H}_2\text{O}$ . The EC/DEC electrolyte mimics real battery testing conditions to determine whether the liquid electrolyte can infiltrate HCS pores, while the saturated  $\text{NaCl}/\text{H}_2\text{O}$  solution is used as an indicator of liquid penetration due to its high salt concentration (relative to 1 M  $\text{LiPF}_6$  in EC/DEC) that will precipitate as the solvent evaporates. Bare HCS electrodes and ALD  $\text{Al}_2\text{O}_3/\text{HCS}$  electrodes were immersed in either battery electrolyte or saturated  $\text{NaCl}/\text{H}_2\text{O}$  solution overnight. Electrodes were then taken out of the solution and gently wiped to remove excess solution on the surface and then dried inside a glove box (electrodes with battery electrolyte) or ambient environment (electrodes with saturated  $\text{NaCl}/\text{H}_2\text{O}$  solution). Both battery electrolyte and saturated  $\text{NaCl}/\text{H}_2\text{O}$  solution entered the HCS cavity and left salt precipitations when dried (Fig. 3, B and C). In contrast, no salt precipitate was identified within ALD  $\text{Al}_2\text{O}_3/\text{HCS}$  cavities for electrodes soaked in both battery electrolyte and  $\text{NaCl}/\text{H}_2\text{O}$  solution. This confirms the feasibility of ALD coatings as a sealant for nanoporous carbon.

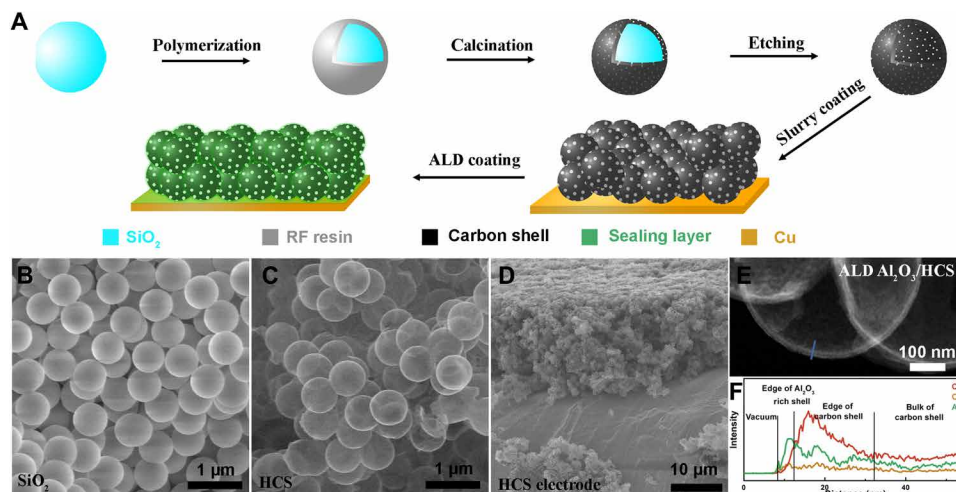


**Fig. 2. Materials synthesis and fabrication.** (A) Schematic of materials synthesis and electrode fabrication processes. (B) SEM characterization of SiO<sub>2</sub> nanoparticles with uniform size distribution. (C) SEM characterization of HCS, with SiO<sub>2</sub> nanoparticle templates being removed by etching. (D) SEM characterization of an electrode with stacked HCS prepared via the typical slurry process. (E and F) STEM image and EDX line scan of ALD Al<sub>2</sub>O<sub>3</sub>/HCS.

Lithium ion conductivity, electrical conductivity, and mechanical strain are important factors that need to be considered when building a 3D host for lithium metal anodes. In the case of ALD-coated HCS electrodes, electrical conductivity mismatch is one driving force for lithium to nucleate on the inner surface of HCS rather than on the outer Al<sub>2</sub>O<sub>3</sub> surface (16, 17). Further, considering mechanical stress, it would be energetically more favorable for lithium to nucleate inside the HCS cavity, which is free of mechanical stress, than to break the Al<sub>2</sub>O<sub>3</sub>/C interface (33). In addition, the lithium ion diffusion coefficient is higher in carbon than in ALD coating layers, which minimizes possible lithium ion accumulation and lithium plating at the Al<sub>2</sub>O<sub>3</sub>/C interface. Previous in situ SEM characterizations have shown that lithium ions prefer to diffuse past a LiPON/C interface and plate as lithium metal on a carbon surface free of mechanical stress (33). To directly visualize the lithium plating morphology, we performed both cross-sectional and planar SEM. The cross-sectional SEM images were obtained using FIB cutting after initial lithium plating, which confirmed that the lithium was able to enter the ALD Al<sub>2</sub>O<sub>3</sub>/HCS cavity and form lithium nuclei (Fig. 3, L and M). For comparison, lithium nucleates both outside and inside the bare HCS due to electrolyte penetration of the hollow cavity (Fig. 3, I and J). Large-area cross-sectional SEM characterization was also provided (see the Supplementary Materials), and no obvious lithium overplating has been observed outside ALD Al<sub>2</sub>O<sub>3</sub>-coated HCS at different depths of the electrode. The exposed surface of a Cu current collector at the bottom of the electrode has also been covered by Al<sub>2</sub>O<sub>3</sub> (see the Supplementary Materials). Because of the strong adhesion between Cu and Al<sub>2</sub>O<sub>3</sub>, no lithium plating took place on an Al<sub>2</sub>O<sub>3</sub>-covered Cu current collector (see the Supplementary Materials). In addition to the cross-sectional SEM, top-view SEM images were acquired for the ALD Al<sub>2</sub>O<sub>3</sub>/HCS electrode after different amounts of lithium plating. No lithium plating outside ALD Al<sub>2</sub>O<sub>3</sub>/HCS can be observed in the top-view SEM images, so long as the cell is limited to its theoretical capacity for the hollow sphere to hold (see the Supplementary Materials).

### Electrochemical performance in carbonate-based electrolyte and discussion of battery failure mechanism

To evaluate the effectiveness of ALD coating, we paired Cu, HCS, and ALD Al<sub>2</sub>O<sub>3</sub>/HCS working electrodes with lithium foil counter electrodes for cycling tests. As one of the most successful electrolytes in commercial lithium ion batteries, the carbonate-based electrolyte was selected as the platform for this study. We performed cycling tests in a limited amount (30  $\mu$ l) of the EC/DEC electrolyte with 1 M LiPF<sub>6</sub>, 1% vinylene carbonate (VC), and 10% fluoroethylene carbonate (FEC) (see Materials and Methods). During each cycle, lithium with a total capacity of 1 mAh/cm<sup>2</sup> was electrochemically plated on the working electrodes with a current density of 2 mA/cm<sup>2</sup>. The HCS electrodes were then cycled to a cutoff potential of 1.0 V versus Li<sup>+</sup>/Li at the same rate of 2 mA/cm<sup>2</sup> to strip the electrochemically deposited lithium. The coulombic efficiency was defined as the Li stripping capacity divided by the Li plating capacity for each cycle, which is a powerful indicator of the stability of the lithium metal anodes over cycling. Despite added VC and FEC additives, the coulombic efficiencies on bare Cu electrodes steadily decreased as cycling progressed, suggesting significant side reactions between plated lithium and the carbonate electrolyte. The coulombic efficiencies were slightly improved when using HCS electrodes, but still unsatisfactory. The bicontinuous structure of HCS provides confined space for lithium plating and could therefore slow down both lithium dendrite growth and parasitic reactions (34, 35). Nevertheless, undesired parasitic reactions may still occur in between exposed lithium and electrolyte. For comparison, ALD Al<sub>2</sub>O<sub>3</sub>/HCS lasted more than 100 cycles in the same amount of 30  $\mu$ l of the electrolyte with a high average coulombic efficiency of more than 96%. In addition, while coulombic efficiencies dropped when switching to the additive-free electrolyte in HCS electrodes, the coulombic efficiencies were similar for ALD Al<sub>2</sub>O<sub>3</sub>/HCS electrodes in both additive-added and additive-free electrolytes (see the Supplementary Materials).

The detailed voltage versus capacity plots of Cu, HCS, and ALD Al<sub>2</sub>O<sub>3</sub>/HCS electrodes were also compared (Fig. 4, B to E). The overpotential for the initial electrochemical plating and stripping of

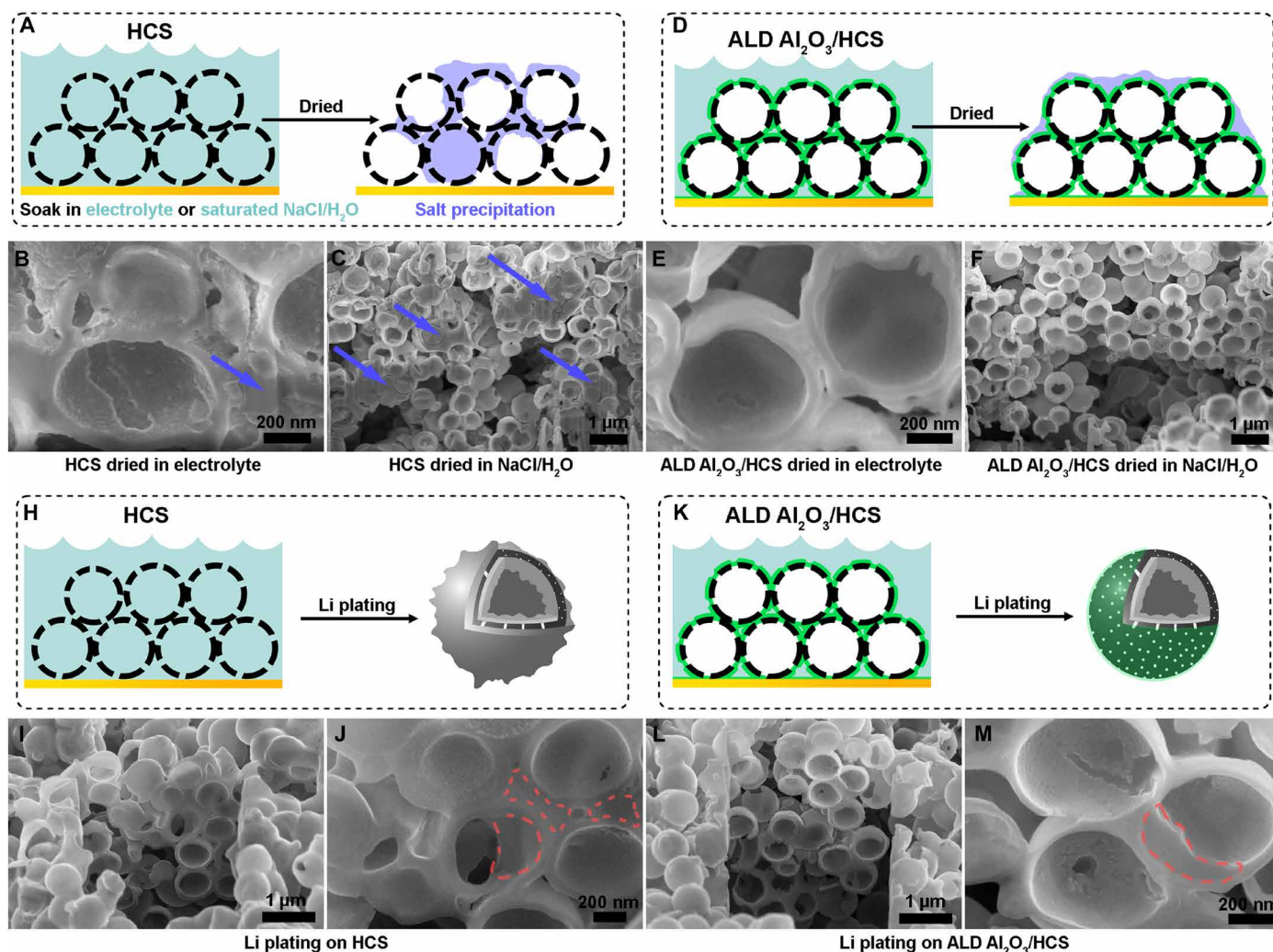


**Fig. 3. Soaking and electrochemical lithium plating experiments.** (A to C) Schematic and SEM of HCS electrodes soaked and dried in 1 M LiPF<sub>6</sub>/EC/DEC electrolyte and saturated NaCl/H<sub>2</sub>O solution. Blue arrows highlight the location of NaCl precipitation. (D to F) Schematic and SEM of ALD Al<sub>2</sub>O<sub>3</sub>/HCS electrodes soaked and dried in 1 M LiPF<sub>6</sub>/EC/DEC electrolyte or saturated NaCl/H<sub>2</sub>O solution. (H to J) Schematic and SEM of HCS electrodes after electrochemical lithium plating in LiPF<sub>6</sub>/EC/DEC electrolyte. Red circles highlight the locations of plated lithium inside and outside HCS. (K to M) Schematic and SEM of ALD Al<sub>2</sub>O<sub>3</sub>/HCS electrodes after electrochemical lithium plating in LiPF<sub>6</sub>/EC/DEC electrolyte. Red circle highlights the location of plated lithium inside ALD Al<sub>2</sub>O<sub>3</sub>/HCS. All electrodes were cut open using FIB for viewing. SEM images were taken with a sample rotation angle of 52°.

lithium was slightly higher in the ALD Al<sub>2</sub>O<sub>3</sub>/HCS electrode than in the HCS electrode (Fig. 4B). This result can be ascribed to two factors. First, compared to the ALD Al<sub>2</sub>O<sub>3</sub>/HCS electrode, the pristine HCS electrode has a higher electrode/electrolyte contact surface area for lithium nucleation because the inner wall of some carbon spheres is also accessible to the electrolyte. The lithium plating could take place everywhere around the carbon sphere. Second, in the case of ALD Al<sub>2</sub>O<sub>3</sub>-coated HCS, the added Al<sub>2</sub>O<sub>3</sub> coating, together with the carbon shell, acts as an artificial SEI layer. It generates a barrier for lithium ions to migrate through and plate inside the spheres.

Here, the segregation of the liquid electrolyte from electrodeposited lithium is of immense importance to the long-term cycling stability of the lithium metal anodes. This is because most battery electrolytes are not stable against lithium metal and form SEI as a side product upon contact. This SEI is not mechanically sturdy enough to suppress lithium morphology changes, including dendrite formation. Therefore,

it continues to form and break upon cycling, leading to the buildup of discarded SEI. To test whether SEI forms in the ALD/HCS electrode, we performed FIB/SEM characterization on cross sections of HCS and ALD Al<sub>2</sub>O<sub>3</sub>/HCS electrodes after cycling. After 25 lithium plating/stripping cycles (last half-cycle is lithium stripping cycle), SEI and/or dead lithium remain in the HCS electrode (Fig. 4F). In ALD Al<sub>2</sub>O<sub>3</sub>/HCS, SEI is not evident within the sphere (Fig. 4G).

The formation of SEI leads to the continuous consumption of both electrolyte and active lithium. In our current half-cell testing setup, as there is excess lithium in the counter electrode, the quick depletion of the electrolyte leads to poor lithium ion conduction and eventually battery failure. To test this hypothesis, cycling tests with different amounts of the added electrolyte were also performed with the HCS working electrodes (Fig. 4H). With a small amount of the added electrolyte (15 μl), the coulombic efficiency dropped to below 70% in less than 15 cycles. On the contrary, if an adequate amount of

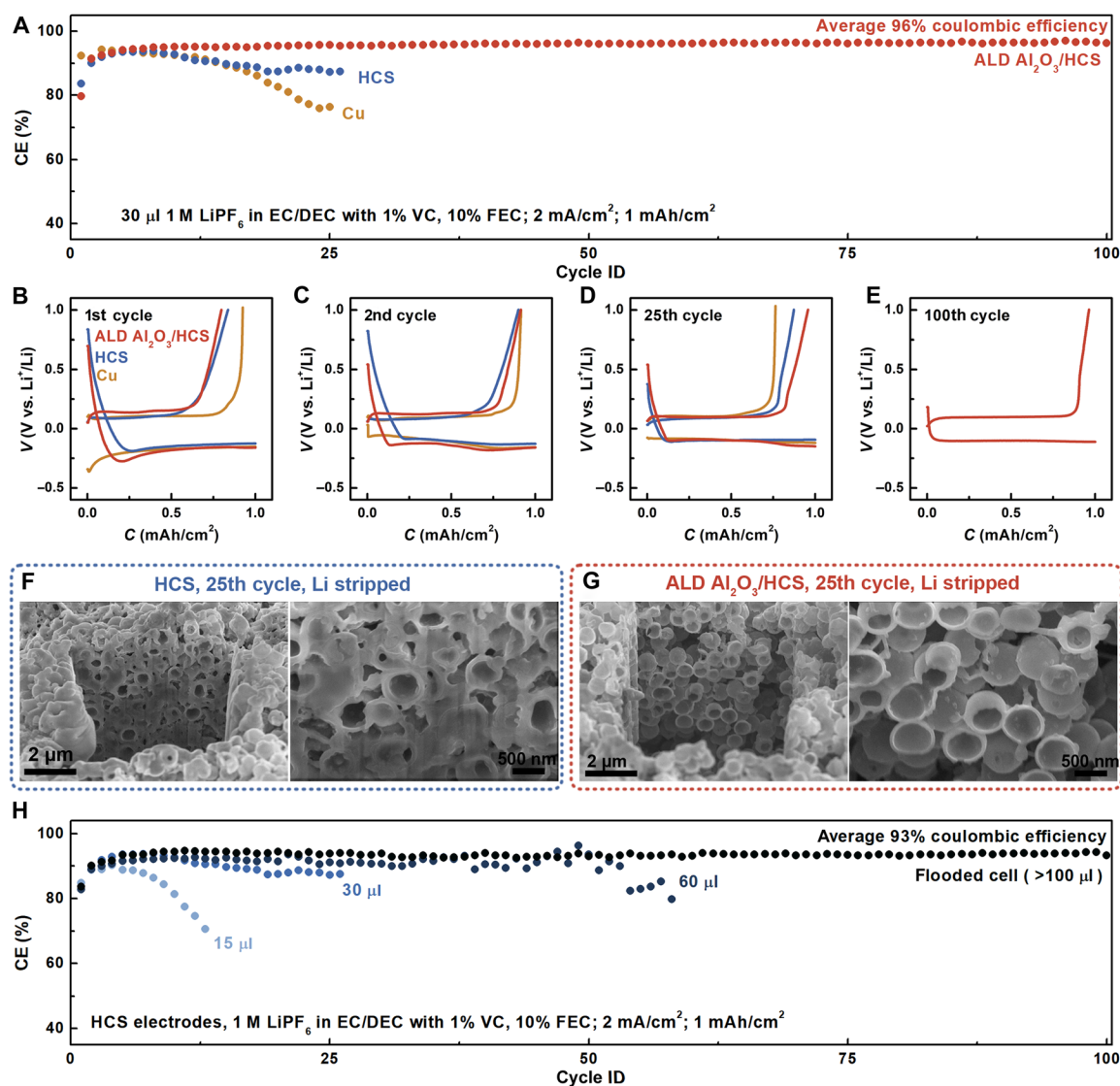


**Fig. 4. Cycling performance in carbonate electrolyte and study of failure mechanisms.** (A) Coulombic efficiency versus cycle number plots of Cu, HCS, and ALD Al<sub>2</sub>O<sub>3</sub>/HCS in 30  $\mu$ l of EC/DEC electrolyte with 1 M LiPF<sub>6</sub>, 1% VC, and 10% FEC. (B to E) Voltage versus capacity plot during 1st, 2nd, 25th, and 100th cycles. (F) SEM characterization of HCS electrodes after 25 cycles. Images were acquired after the last lithium stripping half-cycle. (G) SEM characterization of ALD Al<sub>2</sub>O<sub>3</sub>/HCS electrodes after 25 cycles. Images were acquired after the last lithium stripping half-cycle. (H) Cycling performance of repeated electrochemical Li plating/stripping on HCS electrodes with different amounts of EC/DEC electrolyte containing 1 M LiPF<sub>6</sub>, 1% VC, and 10% FEC. All electrodes were cut open for viewing using FIB. SEM images were taken with a rotation angle of 52°.

the electrolyte was added by flooding the cell (more than 100  $\mu$ l of the electrolyte; see Materials and Methods), then the cycle life can be extended to 100 cycles. Therefore, the clogging of the HCS electrode by SEI debris, together with the consumption of the liquid electrolyte, contributes to the failure of these half-cells. When testing symmetric cells with a limited amount of lithium, the depletion of lithium may serve as an additional cause for cell failure (see the Supplementary Materials). In a practical cell, as both cyclable lithium and electrolyte are limited, it is even more critical to minimize the continuous parasitic reaction between them.

The separation of deposited lithium and liquid electrolyte greatly improved the coulombic efficiency and cycle life of lithium metal anodes. The coulombic efficiency and cycle life of the ALD Al<sub>2</sub>O<sub>3</sub>/HCS electrode is superior compared to the bare HCS electrode with

the same amount of the electrolyte (decreased to <90% within 10 cycles in 30  $\mu$ l of the electrolyte) and the HCS electrode with an excess amount of the electrolyte (~93% in the flooded electrolyte). The reported coulombic efficiency (~96% for more than 100 cycles in 30  $\mu$ l of the carbonate electrolyte) of the ALD Al<sub>2</sub>O<sub>3</sub>/HCS electrode is one of the highest values reported in the literature using the same type of electrolyte under similar cycling conditions. The improved stability is attributed to the ability of the ALD Al<sub>2</sub>O<sub>3</sub>-coated carbon shell to prevent electrolyte penetration inside the electrode, preventing lithium-electrolyte reactions.

#### Electrochemical performance in ether-based electrolyte

The ether-based electrolyte represents another category of promising electrolyte, which has been intensively researched due to its higher

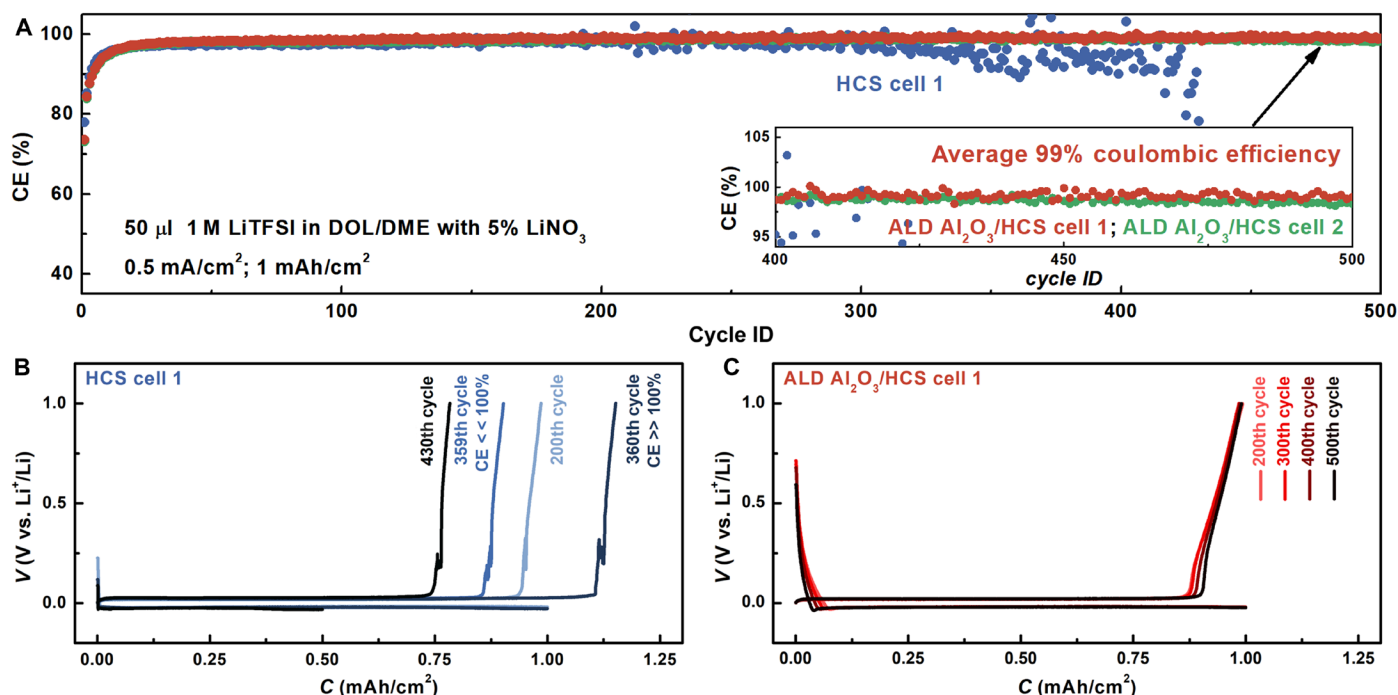


**Fig. 5. Cycling performance in ether electrolyte.** (A) Coulombic efficiency versus cycle number plots of HCS and ALD Al<sub>2</sub>O<sub>3</sub>/HCS cells in 50  $\mu$ l of 1:1 DOL/DME electrolyte with 1 M LiTFSI and 5% LiNO<sub>3</sub>. (B) Voltage versus capacity plot of HCS electrode during 200th, 359th, 360th, and 430th cycles. (C) Voltage versus capacity plot of ALD Al<sub>2</sub>O<sub>3</sub>/HCS electrode during 200th, 300th, 400th, and 500th cycles.

stability compared to the carbonate electrolyte and has been widely adopted in research and development for both Li-S and Li-O<sub>2</sub> batteries (36, 37). The cycle performance of ALD Al<sub>2</sub>O<sub>3</sub>/HCS electrodes was evaluated in 50  $\mu$ l of the ether-based electrolyte consisting of 1 M LiTFSI and 5% LiNO<sub>3</sub> in 1:1 dioxolane (DOL)/dimethoxyethane (DME) electrolyte (cycling tests were also performed in the electrolyte with 2% LiNO<sub>3</sub> as additive; see the Supplementary Materials). Although safety concerns related to the high flammability of the ether electrolyte still need to be solved, the ether-based electrolyte is known for better lithium metal anode cycling behavior when compared to the carbonate-based electrolyte. For pristine HCS electrodes, the coulombic efficiency approached 98% during the first 200 cycles and then began to fluctuate in later cycles (Fig. 5A). More specifically, the coulombic efficiency sometimes reached a low value and then followed with an abnormally high value (>100%) in later cycles. These observations could be related to the formation of dead lithium in the HCS electrode, as the accumulation of SEI debris became evident after many repeated cycles of lithium plating/stripping. Because of the poor electrical conductivity of an accumulated thick layer of SEI debris, once the root of lithium is stripped away during the stripping half-cycle, the remaining part of lithium may break off and lose its electrical connection to the electrode. This process causes the formation of dead lithium and a poor coulombic efficiency in the present cycle. Once the electrical connection was reestablished in the following lithium plating half-cycle, a higher coulombic efficiency was possible. For instance, the coulombic efficiency of the HCS electrode was 90.2% in the 359th cycle and 115.2% in the 360th cycle (Fig. 5B). These fluctuations became more evident toward the end of the HCS electrode's cycle life. For comparison, the coulombic efficiency versus cycle number curve of the two ALD Al<sub>2</sub>O<sub>3</sub>/HCS electrodes was always stable and smooth for the entire

500 cycles (Fig. 5A). The average coulombic efficiency of both ALD Al<sub>2</sub>O<sub>3</sub> HCS electrodes tested was about 99% for 3 months of testing and, to the best of our knowledge, represents one of the most stable lithium metal anodes cycled in ether electrolyte. The ultralong cycle life, along with high coulombic efficiency, demonstrates the importance of avoiding parasitic reactions through segregation of the liquid electrolyte and electrodeposited lithium.

## CONCLUSION

To summarize, we designed and synthesized electrodes with stable interfaces between the electrolyte and cavities that host lithium metal. We demonstrated that an ALD Al<sub>2</sub>O<sub>3</sub> coating guides the electrochemical plating of lithium inside the HCS host. The ALD Al<sub>2</sub>O<sub>3</sub>-coated carbon shell also serves as an effective artificial SEI, which not only prevents the formation of dendritic lithium but also keeps the electrolyte out. The separation of the electrolyte and electrochemically plated lithium is critical in minimizing parasitic reactions between them. As a result, stable cycling with an average coulombic efficiency as high as 99% was obtained in the ether-based electrolyte for more than 500 cycles.

## MATERIALS AND METHODS

### Synthesis of C/SiO<sub>2</sub> nanoparticles

To prepare SiO<sub>2</sub> templates, 200 ml of NH<sub>4</sub>OH, 140 ml of deionized (DI) water, and 500 ml of dehydrated ethanol were mixed together by stirring at a speed of 200 rpm to make solution (a). Sixty milliliters of tetraethoxysilane (TEOS) was mixed with 120 ml of dehydrated ethanol manually to make solution (b). Solution (b) was then quickly poured into solution (a). After stirring for 8 hours, 10 ml of DI water

and 60 ml of TEOS were added successively into the above solution and stirring was kept for another 8 hours. Finally, SiO<sub>2</sub> particles with a size of around 645 nm were collected through centrifugation and washed alternatively with ethanol and DI water for a total of six times. To prepare C/SiO<sub>2</sub>, 1 g of SiO<sub>2</sub> nanoparticles was dispersed in 300 ml of DI water under ultrasonication for 10 to 30 min. Next, 10 ml of cetyl trimethylammonium bromide (CTAB; Sigma-Aldrich, 10 mM) and 1 ml of ammonia (NH<sub>3</sub>·H<sub>2</sub>O; Sigma-Aldrich, 28%) were added to the SiO<sub>2</sub> solution and vigorously stirred for 20 min to ensure the adsorption of CTAB on the cluster surface. Then, 400 mg of resorcinol (Sigma-Aldrich) and 0.56 ml of formaldehyde solution [Sigma-Aldrich, 37 weight % (wt %) in H<sub>2</sub>O] were added and stirred overnight. The RF resin-coated particles were collected by centrifugation and washed with ethanol three times. Finally, the RF shell was carbonized under Ar at 900°C for 2 hours with a temperature ramping rate of 5°C min<sup>-1</sup>.

### Etching of SiO<sub>2</sub> templates

SiO<sub>2</sub> sacrificial templates were removed with HF solution to achieve HCS. Typically, C/SiO<sub>2</sub> nanoparticles were immersed in 10 wt % HF solution for different periods of time (see the Supplementary Materials), followed by centrifugation and ethanol washing three times. The SiO<sub>2</sub> templates can be completely removed after 12 hours of etching. The final HCS were obtained after drying in a vacuum oven.

### Preparation of HCS electrodes

The HCS electrodes were made through the typical slurry-making process. The slurry was stirred in *N*-methylpyrrolidone (Sigma-Aldrich) solvent with 3:1 HCS/polyvinylidene difluoride ratio for 6 hours and then coated onto a Cu current collector through doctor blading. The electrodes were dried in a vacuum oven overnight. Thin-film coatings were applied directly on HCS electrodes using a Savannah S100 ALD system (Ultratech/Cambridge NanoTech) operated under the exposure mode to ensure high uniformity on high-surface area substrates. The Al<sub>2</sub>O<sub>3</sub> deposition consists of alternating pulse and purge of trimethylaluminum (Sigma-Aldrich) and DI water as precursors at a growth temperature of 150°C. A typical pulse, exposure, and purge sequence for trimethylaluminum and DI water was 0.015 s–15 s–40 s–0.015 s–15 s–40 s. The AlF<sub>3</sub> deposition consists of alternating pulse and purge of AlCl<sub>3</sub> (>99%, Sigma-Aldrich) and TiF<sub>4</sub> (grinded before use, Sigma-Aldrich) as precursors at a growth temperature of 200°C. Both AlCl<sub>3</sub> and TiF<sub>4</sub> precursors were kept at 120° to 130°C. A typical pulse, exposure, and purge sequence for AlCl<sub>3</sub> and TiF<sub>4</sub> was 1 s–15 s–30 s–1 s–15 s–30 s.

### Soaking of HCS and ALD/HCS electrodes

To test the permeability of the HCS shell, HCS electrodes and ALD Al<sub>2</sub>O<sub>3</sub>/HCS electrodes were soaked in both battery electrolyte and saturated NaCl/H<sub>2</sub>O solution overnight. Electrodes were then taken out of the liquid. Electrodes soaked in the battery electrolyte were dried inside the glove box, and electrodes soaked in saturated NaCl solution were dried in an ambient environment.

### Electrochemical measurements

Battery cycling performance was evaluated by the galvanostatic cycling of coin cells (CR 2032) with HCS working electrodes and ALD Al<sub>2</sub>O<sub>3</sub>/HCS working electrodes (1 cm<sup>2</sup>, 0.5 mg/cm<sup>2</sup>). Li foils (Alfa Aesar, thickness of 700 μm) were used as the counter electrodes. Two layers of Celgard separators (Celgard 2325, 25 μm thick) were

used to separate the working electrode and the counter electrode. Different amounts of the electrolyte were added to each coin cell, as indicated in the main text. For a flooded coin cell, more than 100 μl of the electrolyte was added until the coin cell reached full capacity. Two types of electrolytes were used: (i) 1 M LiPF<sub>6</sub> in 1:1 (v/v) EC and DEC (BASF) with 1% VC and 10% FEC as additives and (ii) 1 M LiTFSI in 1:1 (v/v) DOL/DME electrolyte with 5% LiNO<sub>3</sub> as additive. Battery cycling data were collected using a LAND eight-channel battery tester at room temperature. After assembly, coin cells were galvanostatically cycled between 0 and 1 V at 200 μA/cm<sup>2</sup> for five cycles. Battery cycling was then performed by controlling an areal capacity of 1 mAh/cm<sup>2</sup> for Li plating and a cutoff potential of 1 V versus Li<sup>+</sup>/Li for Li stripping during each cycle. The coulombic efficiency was defined as the Li stripping capacity divided by the Li plating capacity.

### Materials characterizations

SEM images were captured in a FEI XL30 Sirion SEM. TEM characterization was performed at 300 kV using a FEI Titan TEM. The morphology of plated Li was observed with a FIB (Nova 600i Dual Beam, FEI). The cycled electrodes were cross-sectioned with a Ga<sup>+</sup> ion beam and observed with the SEM (JSM-6700F, JEOL). X-ray photoelectron spectroscopy (XPS) was performed on PHI 5000 VersaProbe, using an Al Kα (λ = 0.83 nm, hν = 1486.7 eV) x-ray source operated at 2 kV and 20 mA.

### SUPPLEMENTARY MATERIALS

Supplementary material for this article is available at <http://advances.sciencemag.org/cgi/content/full/4/7/eaat5168/DC1>

Fig. S1. Etching of C/SiO<sub>2</sub> nanoparticles in HF solution.

Fig. S2. Top-view SEM characterization of HCS electrode and ALD Al<sub>2</sub>O<sub>3</sub> HCS electrode after initial electrochemical lithium plating.

Fig. S3. XPS characterization.

Fig. S4. Cross-sectional SEM characterization of ALD Al<sub>2</sub>O<sub>3</sub>/HCS electrode after lithium plating.

Fig. S5. Optical and SEM images of ALD Al<sub>2</sub>O<sub>3</sub>/HCS electrodes after different amounts of electrochemical lithium plating.

Fig. S6. Cycle performance in carbonate electrolyte with and without additives.

Fig. S7. Cycle performance of symmetric cells.

Fig. S8. Cycle performance in ether electrolyte.

Fig. S9. STEM-EDX line scan of ALD AlF<sub>3</sub>-coated HCS.

Fig. S10. Additional cycle performance data of ALD Al<sub>2</sub>O<sub>3</sub>/HCS and ALD AlF<sub>3</sub>/HCS electrodes.

References (38, 39)

### REFERENCES AND NOTES

1. P. G. Bruce, S. A. Freunberger, L. J. Hardwick, J.-M. Tarascon, Li–O<sub>2</sub> and Li–S batteries with high energy storage. *Nat. Mater.* **11**, 19–29 (2012).
2. J. Lu, L. Li, J.-B. Park, Y.-K. Sun, F. Wu, K. Amine, Aprotic and aqueous Li–O<sub>2</sub> batteries. *Chem. Rev.* **114**, 5611–5640 (2014).
3. Y. Sun, N. Liu, Y. Cui, Promises and challenges of nanomaterials for lithium-based rechargeable batteries. *Nat. Energy* **1**, 16071 (2016).
4. X. Yao, Q. Dong, Q. Cheng, D. Wang, Why do lithium-oxygen batteries fail: Parasitic chemical reactions and their synergistic effect. *Angew. Chem. Int. Ed. Engl.* **55**, 11344–11353 (2016).
5. W. Xu, J. Wang, F. Ding, X. Chen, E. Nasybutin, Y. Zhang, J.-G. Zhang, Lithium metal anodes for rechargeable batteries. *Energy Environ. Sci.* **7**, 513–537 (2014).
6. D. Lin, Y. Liu, Y. Cui, Reviving the lithium metal anode for high-energy batteries. *Nat. Nanotechnol.* **12**, 194–206 (2017).
7. D. Aurbach, E. Zinigrad, H. Teller, P. Dan, Factors which limit the cycle life of rechargeable lithium (metal) batteries. *J. Electrochem. Soc.* **147**, 1274–1279 (2000).
8. D. Aurbach, E. Zinigrad, Y. Cohen, H. Teller, A short review of failure mechanisms of lithium metal and lithiated graphite anodes in liquid electrolyte solutions. *Solid State Ion.* **148**, 405–416 (2002).
9. Z. Liang, D. Lin, J. Zhao, Z. Lu, Y. Liu, C. Liu, Y. Lu, H. Wang, K. Yan, X. Tao, Y. Cui, Composite lithium metal anode by melt infusion of lithium into a 3D conducting scaffold with lithiophilic coating. *Proc. Natl. Acad. Sci. U.S.A.* **113**, 2862–2867 (2016).

10. D. Lin, Y. Liu, Z. Liang, H.-W. Lee, J. Sun, H. Wang, K. Yan, J. Xie, Y. Cui, Layered reduced graphene oxide with nanoscale interlayer gaps as a stable host for lithium metal anodes. *Nat. Nanotechnol.* **11**, 626–632 (2016).
11. Y. Liu, D. Lin, Z. Liang, J. Zhao, K. Yan, Y. Cui, Lithium-coated polymeric matrix as a minimum volume-change and dendrite-free lithium metal anode. *Nat. Commun.* **7**, 10992 (2016).
12. K. Yan, Z. Lu, H.-W. Lee, F. Xiong, P.-C. Hsu, Y. Li, J. Zhao, S. Chu, Y. Cui, Selective deposition and stable encapsulation of lithium through heterogeneous seeded growth. *Nat. Energy* **1**, 16010 (2016).
13. S. Liu, A. Wang, Q. Li, J. Wu, K. Chiou, J. Huang, J. Luo, Crumpled graphene balls stabilized dendrite-free lithium metal anodes. *Joule* **2**, 184–193 (2018).
14. X. W. Lou, L. A. Archer, Z. Yang, Hollow micro-/nanostructures: Synthesis and applications. *Adv. Mater.* **20**, 3987–4019 (2008).
15. X. Wang, J. Feng, Y. Bai, Q. Zhang, Y. Yin, Synthesis, properties, and applications of hollow micro-/nanostructures. *Chem. Rev.* **116**, 10983–11060 (2016).
16. A. C. Cozen, C.-F. Lin, A. J. Pearse, M. A. Schroeder, X. Han, L. Hu, S.-B. Lee, G. W. Rubloff, M. Noked, Next-generation lithium metal anode engineering via atomic layer deposition. *ACS Nano* **9**, 5884–5892 (2015).
17. E. Kazyak, K. N. Wood, N. P. Dasgupta, Improved cycle life and stability of lithium metal anodes through ultrathin atomic layer deposition surface treatments. *Chem. Mater.* **27**, 6457–6462 (2015).
18. Y. Zhang, B. Liu, E. Hitz, W. Luo, Y. Yao, Y. Li, J. Dai, C. Chen, Y. Wang, C. Yang, H. Li, L. Hu, A carbon-based 3D current collector with surface protection for Li metal anode. *Nano Res.* **10**, 1356–1365 (2017).
19. S. Choudhury, L. A. Archer, Lithium fluoride additives for stable cycling of lithium batteries at high current densities. *Adv. Electron. Mater.* **2**, 1500246 (2016).
20. L. Fan, H. L. Zhuang, L. Gao, Y. Lu, L. A. Archer, Regulating Li deposition at artificial solid electrolyte interphases. *J. Mater. Chem. A* **5**, 3483–3492 (2017).
21. N.-W. Li, Y.-X. Yin, C.-P. Yang, Y.-G. Guo, An artificial solid electrolyte interphase layer for stable lithium metal anodes. *Adv. Mater.* **28**, 1853–1858 (2016).
22. Q. Pang, X. Liang, A. Shyamsunder, L. F. Nazar, An in vivo formed solid electrolyte surface layer enables stable plating of Li metal. *Joule* **1**, 871–886 (2017).
23. J. Xie, L. Liao, Y. Gong, Y. Li, F. Shi, A. Pei, J. Sun, R. Zhang, B. Kong, R. Subbaraman, J. Christensen, Y. Cui, Stitching h-BN by atomic layer deposition of LiF as a stable interface for lithium metal anode. *Sci. Adv.* **3**, eaao3170 (2017).
24. K. Yan, H.-W. Lee, T. Gao, G. Y. Zheng, H. Yao, H. Wang, Z. Lu, Y. Zhou, Z. Liang, Z. Liu, S. Chu, Y. Cui, Ultrathin two-dimensional atomic crystals as stable interfacial layer for improvement of lithium metal anode. *Nano Lett.* **14**, 6016–6022 (2014).
25. K. Fu, Y. Gong, B. Liu, Y. Zhu, S. Xu, Y. Yao, W. Luo, C. Wang, S. D. Lacey, J. Dai, Y. Chen, Y. Mo, E. Wachsman, L. Hu, Toward garnet electrolyte-based Li metal batteries: An ultrathin, highly effective, artificial solid-state electrolyte/metallic Li interface. *Sci. Adv.* **3**, e1601659 (2017).
26. J. Xie, A. D. Sendek, E. D. Cubuk, X. Zhang, Z. Lu, Y. Gong, T. Wu, F. Shi, W. Liu, E. J. Reed, Y. Cui, Atomic layer deposition of stable LiAlF<sub>4</sub> lithium ion conductive interfacial layer for stable cathode cycling. *ACS Nano* **11**, 7019–7027 (2017).
27. J. Xie, J. Zhao, Y. Liu, H. Wang, C. Liu, T. Wu, P.-C. Hsu, D. Lin, Y. Jin, Y. Cui, Engineering the surface of LiCoO<sub>2</sub> electrodes using atomic layer deposition for stable high-voltage lithium ion batteries. *Nano Res.* **10**, 3754–3764 (2017).
28. A. H. Moreno, A. Arenillas, E. G. Calvo, J. M. Bermúdez, J. A. Menéndez, Carbonisation of resorcinol–formaldehyde organic xerogels: Effect of temperature, particle size and heating rate on the porosity of carbon xerogels. *J. Anal. Appl. Pyrolysis* **100**, 111–116 (2013).
29. X. Li, S. Bai, Z. Zhu, J. Sun, X. Jin, X. Wu, J. Liu, Hollow carbon spheres with abundant micropores for enhanced CO<sub>2</sub> adsorption. *Langmuir* **33**, 1248–1255 (2017).
30. C. Goel, H. Bhunia, P. K. Bajpai, Resorcinol–formaldehyde based nanostructured carbons for CO<sub>2</sub> adsorption: Kinetics, isotherm and thermodynamic studies. *RSC Adv.* **5**, 93563–93578 (2015).
31. R. G. Gordon, D. Hausmann, E. Kim, J. Shepard, A kinetic model for step coverage by atomic layer deposition in narrow holes or trenches. *Chem. Vap. Deposition* **9**, 73–78 (2003).
32. Y.-B. Jiang, N. Liu, H. Gerung, J. L. Cecchi, C. J. Brinker, Nanometer-thick conformal pore sealing of self-assembled mesoporous silica by plasma-assisted atomic layer deposition. *J. Am. Chem. Soc.* **128**, 11018–11019 (2006).
33. A. Yulaev, V. Oleshko, P. Haney, J. Liu, Y. Qi, A. A. Talin, M. S. Leite, A. Kolmakov, From microparticles to nanowires and back: Radical transformations in plated Li metal morphology revealed via in situ scanning electron microscopy. *Nano Lett.* **18**, 1644–1650 (2018).
34. X. Ke, Y. Cheng, J. Liu, L. Liu, N. Wang, J. Liu, C. Zhi, Z. Shi, Z. Guo, Hierarchically bicontinuous porous copper as advanced 3D skeleton for stable lithium storage. *ACS Appl. Mater. Interfaces* **10**, 13552–13561 (2018).
35. D. Li, L. Chen, T. Wang, L.-Z. Fan, 3D fiber-network-reinforced bicontinuous composite solid electrolyte for dendrite-free lithium metal batteries. *ACS Appl. Mater. Interfaces* **10**, 7069–7078 (2018).
36. J. Xie, X. Yao, I. P. Madden, D.-E. Jiang, L.-Y. Chou, C.-K. Tsung, D. Wang, Selective deposition of Ru nanoparticles on TiSi<sub>2</sub> nanonet and its utilization for Li<sub>2</sub>O<sub>2</sub> formation and decomposition. *J. Am. Chem. Soc.* **136**, 8903–8906 (2014).
37. S. A. Freunberger, Y. Chen, N. E. Drewett, L. J. Hardwick, F. Bardé, P. G. Bruce, The lithium–oxygen battery with ether-based electrolytes. *Angew. Chem. Int. Ed.* **50**, 8609–8613 (2011).
38. K. R. Williams, R. S. Muller, Etch rates for micromachining processing. *J. Microelectromech. Syst.* **5**, 256–269 (1996).
39. K. R. Williams, K. Gupta, M. Wasilik, Etch rates for micromachining processing-Part II. *J. Microelectromech. Syst.* **12**, 761–778 (2003).

#### Acknowledgments

**Funding:** Part of this work was performed at the Stanford Nano Shared Facilities. This work was sponsored, in part, by Robert Bosch LLC through Bosch Energy Research Network grant no. 03.25.SS.15. The work was partially supported by the Assistant Secretary for Energy Efficiency and Renewable Energy, Office of Vehicle Technologies of the U.S. Department of Energy under the Battery Materials Research (BMR) program and the Battery 500 Consortium program. **Author contributions:** J.X., J.W., and Y.C. conceived and designed the experiments. J.X. and J.W. performed the experiments. H.R.L. and W.H. conducted TEM characterization. F.S. performed FIB test. J.X., J.W., and Y.C. co-wrote the paper. All authors discussed the results and commented on the manuscript. **Competing interests:** Y.C., J.X., and J.W. are inventors on a U.S. Provisional Patent Application filed by the Board of Trustees of the Leland Stanford Junior University that is related to this work (no. 62/668544, filing date: 8 May 2018). The authors declare no other competing interests. **Data and materials availability:** All data needed to evaluate the conclusions in the paper are present in the paper and/or the Supplementary Materials. Additional data related to this paper may be requested from the authors.

Submitted 7 March 2018

Accepted 18 June 2018

Published 27 July 2018

10.1126/sciadv.aat5168

**Citation:** J. Xie, J. Wang, H. R. Lee, K. Yan, Y. Li, F. Shi, W. Huang, A. Pei, G. Chen, R. Subbaraman, J. Christensen, Y. Cui, Engineering stable interfaces for three-dimensional lithium metal anodes. *Sci. Adv.* **4**, eaat5168 (2018).

## Engineering stable interfaces for three-dimensional lithium metal anodes

Jin Xie, Jiangyan Wang, Hye Ryoung Lee, Kai Yan, Yuzhang Li, Feifei Shi, William Huang, Allen Pei, Gilbert Chen, Ram Subbaraman, Jake Christensen and Yi Cui

*Sci Adv* 4 (7), eaat5168.  
DOI: 10.1126/sciadv.aat5168

ARTICLE TOOLS	<a href="http://advances.sciencemag.org/content/4/7/eaat5168">http://advances.sciencemag.org/content/4/7/eaat5168</a>
SUPPLEMENTARY MATERIALS	<a href="http://advances.sciencemag.org/content/suppl/2018/07/23/4.7.eaat5168.DC1">http://advances.sciencemag.org/content/suppl/2018/07/23/4.7.eaat5168.DC1</a>
REFERENCES	This article cites 39 articles, 4 of which you can access for free <a href="http://advances.sciencemag.org/content/4/7/eaat5168#BIBL">http://advances.sciencemag.org/content/4/7/eaat5168#BIBL</a>
PERMISSIONS	<a href="http://www.sciencemag.org/help/reprints-and-permissions">http://www.sciencemag.org/help/reprints-and-permissions</a>

Use of this article is subject to the [Terms of Service](#)

---

*Science Advances* (ISSN 2375-2548) is published by the American Association for the Advancement of Science, 1200 New York Avenue NW, Washington, DC 20005. 2017 © The Authors, some rights reserved; exclusive licensee American Association for the Advancement of Science. No claim to original U.S. Government Works. The title *Science Advances* is a registered trademark of AAAS.